RESEARCH ARTICLE

WILEY

Impact of *b*-value on estimates of apparent fibre density

Sila Genc[1] | **Chantal M. W. Tax[1]** | **Erika P. Raven[1]** | **Maxime Chamberland[1]** | **Greg D. Parker[1,2]** | **Derek K. Jones[1,3]**

[1]Cardiff University Brain Research Imaging Centre (CUBRIC), School of Psychology, Cardiff University, Wales, UK

[2]Experimental MRI Centre (EMRIC), School of Biosciences, Cardiff University, Wales, UK

[3]Mary MacKillop Institute for Health Research, Australian Catholic University, Melbourne, Australia

Correspondence
Sila Genc, Cardiff University Brain Research Imaging Centre (CUBRIC), Cardiff University, Cardiff CF24 4HQ, UK.
Email: gencs@cardiff.ac.uk

Abstract

Recent advances in diffusion magnetic resonance imaging (dMRI) analysis techniques have improved our understanding of fibre-specific variations in white matter microstructure. Increasingly, studies are adopting multi-shell dMRI acquisitions to improve the robustness of dMRI-based inferences. However, the impact of *b*-value choice on the estimation of dMRI measures such as apparent fibre density (AFD) derived from spherical deconvolution is not known. Here, we investigate the impact of *b*-value sampling scheme on estimates of AFD. First, we performed simulations to assess the correspondence between AFD and simulated intra-axonal signal fraction across multiple *b*-value sampling schemes. We then studied the impact of sampling scheme on the relationship between AFD and age in a developmental population (n = 78) aged 8–18 (mean = 12.4, SD = 2.9 years) using hierarchical clustering and whole brain fixel-based analyses. Multi-shell dMRI data were collected at 3.0T using ultra-strong gradients (300 mT/m), using 6 diffusion-weighted shells ranging from b = 0 to 6,000 s/mm^2. Simulations revealed that the correspondence between estimated AFD and simulated intra-axonal signal fraction was improved with high *b*-value shells due to increased suppression of the extra-axonal signal. These results were supported by in vivo data, as sensitivity to developmental age-relationships was improved with increasing *b*-value (*b* = 6,000 s/mm^2, median R^2 = .34; *b* = 4,000 s/mm^2, median R^2 = .29; *b* = 2,400 s/mm^2, median R^2 = .21; *b* = 1,200 s/mm^2, median R^2 = .17) in a tract-specific fashion. Overall, estimates of AFD and age-related microstructural development were better characterised at high diffusion-weightings due to improved correspondence with intra-axonal properties.

KEYWORDS

apparent fibre density, constrained spherical deconvolution, development, diffusion MRI, fixel based analysis, white matter

1 | INTRODUCTION

Diffusion magnetic resonance imaging (dMRI; Le Bihan & Breton, 1985) offers a magnified window into white matter by probing the tissue microstructure properties. Various dMRI modelling and analysis techniques are available, which aim to summarise the local architecture of white matter

as a quantitative metric. However, the biological interpretations around commonly investigated dMRI metrics rest heavily on whether the acquisition protocol can capture the relevant microstructural attributes (Lebel & Deoni, 2018; Tournier, Mori, & Leemans, 2011).

Traditionally, studies have acquired dMRI data with one diffusion-weighting (or *b*-value shell), opting for either low *b*-values

(e.g., b = 1,000 s/mm^2) for diffusion tensor imaging (DTI) analyses (Jones, Horsfield, & Simmons, 1999; Landman et al., 2007), or moderate-to-high b-values (e.g., $b \geq 3,000$ s/mm^2) for probabilistic tractography (Tournier, Calamante, & Connelly, 2013). More recently, with the advent of multi-slice accelerated imaging (Barth, Breuer, Koopmans, Norris, & Poser, 2016), the acquisition of multiple dMRI shells has become more feasible. This has considerably improved data acquisition capabilities for sensitive populations (such as children and clinical populations) which may not withstand long acquisition times (Kunz et al., 2014; Silk et al., 2016; Somerville et al., 2018).

Multi-shell dMRI data has been used in conjunction with various analysis approaches (Novikov, Veraart, Jelescu, & Fieremans, 2018; Zhang, Schneider, Wheeler-Kingshott, & Alexander, 2012) across a variety of applications (Genc, Malpas, Ball, Silk, & Seal, 2018; Kunz et al., 2014; Pines et al., 2019). Measures derived from constrained spherical deconvolution (CSD; Dell'Acqua & Tournier, 2019) can infer the intra-axonal signal fraction along multiple fibre pathways (Dell'Acqua, Simmons, Williams, & Catani, 2013; Raffelt et al., 2012). One such measure of microstructural organisation, termed apparent fibre density (AFD), can indicate relative differences in the white matter fibre density per unit volume of tissue. Given that the specificity to the intra-axonal water signal is maximised at high b-values due to higher restriction of water diffusion (Figure 1), AFD can be sensitive to axon density at high diffusion-weightings (Raffelt et al., 2012).

Analysis frameworks such as fixel-based analysis (FBA; Raffelt et al., 2017) provide a means to test fibre-specific differences in AFD within a population. FBA offers two major advantages over alternative dMRI analysis techniques: sensitivity to fibre properties (density and morphology), and specificity to *fi*bre populations within vo*xel*s (or "*fixels*"). This combination of improved sensitivity and specificity increases the possibility of assigning group differences in fibre properties to specific fibre populations (Dimond et al., 2019; Gajamange et al., 2018; Genc et al., 2018; Mito et al., 2018).

In practise, FBA is compatible with both single-shell (Dhollander, Raffelt, & Connelly, 2016) and multi-shell (Jeurissen, Tournier, Dhollander, Connelly, & Sijbers, 2014) dMRI data. An intuitive choice might be to use all available dMRI data to compute fibre-specific AFD. However, this might not be compatible with the underlying assumptions of AFD reflecting intra-axonal properties. In addition, sensitivity to the extra-axonal signal upon the inclusion of lower b-values can influence the response function choice, resulting in a potential mismatch between the response function and the true underlying fibre properties.

Combining FBA with the very latest in MRI gradient hardware (300 mT/m) (Jones et al., 2018), we explore the impact of sampling scheme on AFD estimates using a rich developmental dataset comprising multi-shell diffusion MRI data with b-values ranging from 0 to 6,000 s/mm^2. Firstly, we simulate multiple fibre geometries to showcase how discrepancies in "true" microstructural configurations can influence the interpretations of AFD generated from both single-shell and multi-shell dMRI data. We then conduct experiments to confirm the theory that AFD is more sensitive and specific to axon density at higher b-values, demonstrated by sensitivity to detecting age-relationships in a developmental population of children and adolescents.

2 | METHODS

2.1 | Simulations

Single fibre populations were simulated with the intra- and extra-axonal spaces represented by axially symmetric tensors; the second and third eigenvalues were set to zero for the intra-axonal tensor and equal but non-zero for the extra-axonal tensor (Jespersen, Kroenke, Ostergaard, Ackerman, & Yablonskiy, 2007; Kroenke, Ackerman, & Yablonskiy, 2004). The intra-axonal and extra-axonal parallel diffusivities were set to 1.9 μm^2/ms, and 42 different combinations were simulated with intra-axonal signal fraction f = [0.2,0.3,0.4,0.5,0.6,0.7,0.8] and extra-axonal perpendicular diffusivity $D_{e,\perp}$ = [0.2,0.4,0.6,0.8,1, 1.2] μm^2/ms. 100 Rician noise generalisations were computed with three different signal-to-noise ratio (SNR) values on the b = 0 signal (SNR = 50; 35; and 20). The response function, which should reflect the properties of a single fibre population (Tax, Jeurissen, Vos, Viergever, & Leemans, 2014), was set to have f = 0.3 and $D_{e,\perp}$ = 0.8 μm^2/ms informed by values estimated from the group-wise response function used in this study. These values are in the

b = 0   b = 500   b = 1200   b = 2400   b = 4000   b = 6000
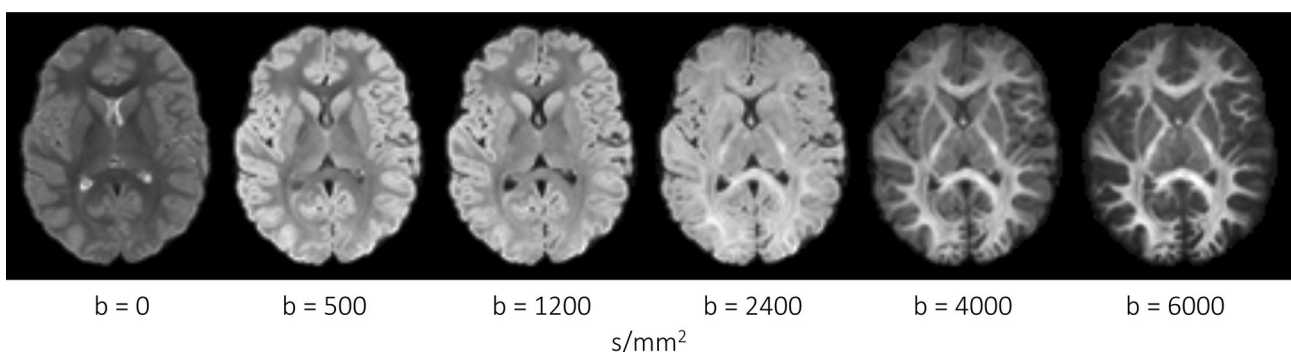
s/mm^2

FIGURE 1 Spherical harmonics (zero order) maps derived from a representative participant (aged 8 years). Visually, increasing b-value from 0 to 6,000 s/mm^2 leads to greater specificity to the signal attributed to the intra-axonal space

range of previously reported estimates of white matter in vivo (Fieremans, Jensen, & Helpern, 2011; Novikov et al., 2018).

2.2 | Participants

We scanned a sample of typically developing children aged 8–18 years recruited as part of the Cardiff University Brain Research Imaging Centre (CUBRIC) Kids study (Genc et al., 2019; Raven et al., 2019). This study was approved by the School of Psychology ethics committee at Cardiff University. Participants and their parents/guardians were recruited via public outreach events. Written informed consent was provided by the primary caregiver of each child participating in the study, and adolescents aged 16–18 years additionally provided written consent. Children were excluded from the study if they had nonremovable metal implants, and if they reported history of a major head injury or epilepsy. All procedures were completed in accordance with the Declaration of Helsinki.

A total of 78 children between the ages of 8–18 years (Mean = 12.4, SD = 2.9 years) were included in the current study (45 female).

2.3 | Diffusion magnetic resonance imaging

2.3.1 | Image acquisition and pre-processing

Diffusion MRI data were acquired on a 3.0T Siemens Connectom system with ultra-strong (300 mT/m) gradients. Multi-shell dMRI data were collected using the following parameters: TE/TR = 59/3000 ms; voxel size = $2 \times 2 \times 2$ mm; b-values = 0 (14 volumes, interleaved), 500 (30 directions), 1,200 (30 directions), 2,400 (60 directions), 4,000 (60 directions), and 6,000 (60 directions) s/mm^2. The larger number of volumes across the higher diffusion weightings were to compensate for lower SNR and to capture the higher angular resolution present at higher b-values (Tournier et al., 2013). Diffusion MRI data were acquired using electrostatic repulsion generalised across multiple shells (Caruyer, Lenglet, Sapiro, & Deriche, 2013). Data were acquired in an anterior–posterior (AP) phase-encoding direction, with one additional PA volume. The total acquisition time (across four acquisition blocks) was 16 min and 14 s.

Pre-processing of dMRI data involved steps largely in line with recommended steps for standard 3.0T systems, interfacing various tools such as FSL (Smith et al., 2004), MRtrix3 (Tournier et al., 2019), and ANTS (Avants et al., 2011). These steps included: denoising (Veraart, Fieremans, & Novikov, 2016), slicewise outlier detection (SOLID; Sairanen, Leemans, & Tax, 2018), and correction for drift (Vos et al., 2017); motion, eddy, and susceptibility-induced distortions (Andersson, Skare, & Ashburner, 2003; Andersson & Sotiropoulos, 2016); Gibbs ringing artefact (Kellner, Dhital, Kiselev, & Reisert, 2016); bias field (Tustison et al., 2010); and gradient nonlinearities (Glasser et al., 2013; Rudrapatna, Parker, Roberts, & Jones, 2018). Root mean squared (RMS) displacement from *eddy* (Andersson & Sotiropoulos, 2016) was used as a summary measure of global head motion. Estimates of SNR were performed by taking the signal in the white matter and dividing this by the

signal outside of the brain (for each b = 0 image). SNR estimates in the in vivo data were: mean = 48.02, SD = 7.46.

2.3.2 | Image processing and analysis

To compare multiple sampling schemes, pre-processed dMRI data were further processed and analysed separately for each sampling scheme in a common population-template space, using a recommended framework (Raffelt et al., 2017). Firstly, data were intensity normalised and spatially upsampled to 1.3 mm^3 isotropic voxel size to increase anatomical contrast and improve tractography (Dyrby et al., 2014). For single-shell (ss) single-tissue constrained spherical deconvolution (CSD), a fibre orientation distribution (FOD; Tournier, Calamante, & Connelly, 2007) was estimated in each voxel with maximal spherical harmonics order l_{max} = 8 for shells with high angular resolution (b = 2,400, 4,000, 6,000 s/mm^2 – 60 directions each) and l_{max} = 6 for shells with lower angular resolution (b = 1,200 s/mm^2 – 30 directions). Multi-shell (ms) multi-tissue CSD was performed using a separate framework (Dhollander et al., 2016; Jeurissen et al., 2014). Following FOD estimation, we derived a population template using all diffusion volumes (ms$_{all}$), and subsequently registered subject-specific and sampling-scheme-specific FOD maps to this template (Figure S1). We then computed an apparent fibre density (AFD) map containing fibre-specific AFD along each fixel for each subject (Raffelt et al., 2017).

In order to estimate AFD along various commonly investigated white matter fibre pathways, white matter tract segmentation was performed. We applied the automated *TractSeg* technique (Wasserthal, Neher, Hirjak, & Maier-Hein, 2019; Wasserthal, Neher, & Maier-Hein, 2018) in population template space, as this technique provides a balance between manual dissection and atlas-based tracking approaches. Of the existing library of 72 tracts, we chose to delineate 38 commonly investigated fibre pathways bilaterally for the left (L) and right (R) hemisphere (Figure S2). This included: AF: arcuate fasciculus; ATR: anterior thalamic radiation; CA: anterior commissure; CC: corpus callosum [1 = rostrum, 2 = genu, 3 = rostral body, 4 = anterior midbody, 5 = posterior midbody; 6 = isthmus, 7 = splenium]; CG = cingulum; CST: corticospinal tract; FX: fornix; ICP: inferior cerebellar peduncle; IFOF: inferior fronto-occipital fasciculus; ILF: inferior longitudinal fasciculus; MCP: middle cerebellar peduncle; MLF: middle longitudinal fasciculus; OR: optic radiation; superior longitudinal fasciculus: SLF [I, II, III]; and UF: uncinate fasciculus. Each tractography map was converted to a fixel map to segment fixels corresponding to streamlines, and AFD was computed within each tract-specific fixel map for further statistical analysis.

2.4 | Statistical analyses

2.4.1 | Impact of b-value sampling scheme

Statistical analyses were performed within R (v3.4.3) and visualisations were carried out in RStudio (v1.2.1335). The coefficient of

determination (R^2) was computed to summarise the proportion of variance explained by age for each sampling-scheme in each tract. Linear models were computed, whereby AFD in each tract was entered as the dependent variable, age was entered as the independent variable, and sex and RMS displacement were set as nuisance variables. To compare sampling schemes in terms of their relationship with age, the difference in R^2 was bootstrapped with 10,000 samples to compute 95% bias corrected accelerated (BCa) confidence intervals.

Hierarchical clustering was performed to discern clusters of sensitivity to age-relationships across various combinations of *b*-value sampling schemes and white matter tracts. These results were visualised as a heatmap with hierarchical clustering using the "*gplots*" package (Warnes et al., 2015) using Euclidean distance and complete agglomeration for clustering. To account for family-wise error (FWE) we made use of a strict Bonferroni correction by adjusting our *p*-value threshold by the 152 comparisons (38 tracts × 4 sampling schemes). As a result, our statistical significance was defined as $p < 3.3e\text{-}4$.

2.4.2 | Whole-brain fixel-based analysis

Separate statistical analyses were performed for each single-shell sampling scheme (*b* = 1,200; 2,400; 4,000; 6,000 s/mm^2) using connectivity-based fixel enhancement (CFE), which provides a permutation-based, family-wise error (FWE) corrected *p*-value for every individual fixel in the template image (Raffelt et al., 2015). For each sampling scheme, we tested the relationship between AFD and age, covarying for sex. For these whole-brain analyses, statistical significance was defined as $p_{FWE} < .05$. Statistically significant fixels were converted into binary fixel maps, and an intersection mask was computed to quantify the proportion of significant fixels overlapping between sampling schemes.

3 | RESULTS

3.1 | Simulations

The results of the simulations for AFD across various fibre geometries and sampling schemes is summarised in Figure 2. Compared to the highest single shell acquisition (ss$_{6000}$), we observe a statistically significant three-way interaction between $D_{e,\perp}$, *f*, and sampling-scheme for ss$_{1200}$: β [95% CI] = .80 [.44, 1.2]; ss$_{2400}$: β [95% CI] = .55 [.19, .91]; ms$_{all}$: β [95% CI] = .83 [.47, 1.2]. These observed differences are visually reflected by a greater dependency of AFD and *f* on simulated $D_{e,\perp}$ as a result of the discrepancy with the response function.

When considering the full multi-shell acquisition (ms$_{all}$) there are multiple degenerate scenarios whereby different combinations of *f* and $D_{e,\perp}$ could result in the same AFD, compared with high *b*-value shells (i.e., ss$_{4000}$ or ss$_{6000}$). From the simulated scenarios for example, if AFD (ms$_{all}$) = 1.2, it can be seen that there are at least six combinations of *f* and $D_{e,\perp}$ resulting in this value (Figure 2). Whereas a change
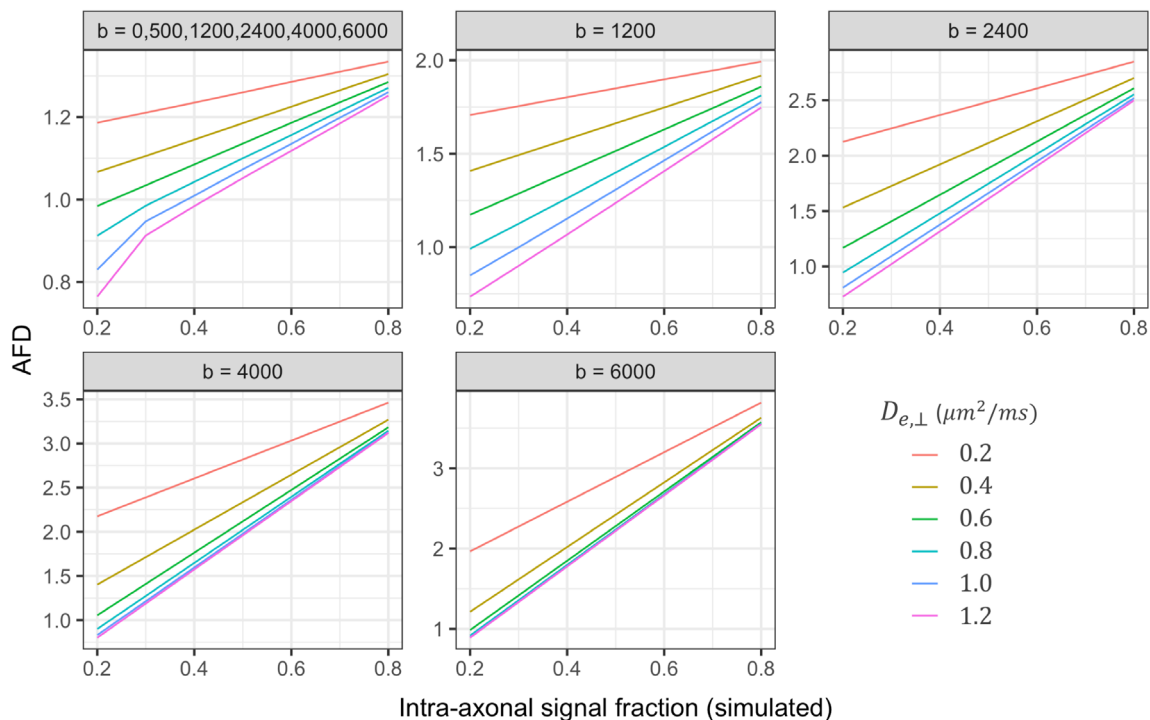
FIGURE 2 AFD for simulated fibre geometries across five sampling schemes. Variations to simulated intra-axonal signal fraction and perpendicular diffusivity of the extra-axonal space ($D_{e,\perp}$) were tested to compare AFD across multiple fibre geometries. Sampling schemes reflect the chosen *b*-values, in s/mm^2

in AFD computed from the highest b-value shell could more directly reflect a change in the underlying f, reducing the potentially confounding effect of discrepancies with the response function.

The addition of noise had negligible effects on these relationships (Figure S3). However, we observed that with decreasing SNR (greater noise), the estimated AFD was more variable.

3.2 | In vivo developmental data

3.2.1 | Impact of b-value sampling scheme

In order to assess the impact of b-value sampling-schemes on tract-specific age relationships, we visualise our data as a heatmap (Figure 3; S4). The coefficient of determination (R^2) derived from the linear model for each tract is organised into hierarchical clusters with branching dendrograms.

3.2.2 | Single-shell single-tissue FBA

We observe two main clusters of single-shell b-value sampling-schemes: the first including low and moderate diffusion-weightings (b = 1,200; 2,400 s/mm^2); and the second including high diffusion-weightings (b = 4,000; 6,000 s/mm^2). Secondly, two tract-specific hierarchical clusters are observed, represented by branching dendrograms (Figure 3: clusters 1 and 2a,b). Sensitivity to age relationships was improved at high diffusion-weightings (Table 1), whereby AFD exhibited a significantly stronger relationship with age at ss_{6000} compared with: ss_{4000} (6/38 tracts); ss_{2400} (25/38 tracts); and ss_{1200} (27/38 tracts).

The first tract cluster is composed of a sub-cluster of regions where a high proportion of age-related variance is described across all diffusion weightings (median R^2 = .40). The first sub-cluster (Figure 3: cluster 1) includes several association tracts (left MLF, bilateral IFOF, left SLF II, bilateral SLF III, bilateral ATR, bilateral AF) and commissural tracts (corpus callosum: full extent, genu, rostral body). Significant age-relationships are observed for all of the sampling schemes (b = 1,200; 2,400; 4,000; 6,000 s/mm^2), with an increase in the estimated R^2 when going to higher diffusion weightings (Figure 4). The proportion of variance explained for the high diffusion-weightings (b = 4,000 and 6,000 s/mm^2) ranged from 38% to 53% (Table 1). Despite the consistent sensitivity to age-related development in this tract cluster, a greater b-value dependence on these relationships was observed when moving from low to high b-values, particularly for association tracts such as bilateral SLF III, left SLF I, left IFOF and left MLF.

The second tract cluster is composed of a sub-cluster (Figure 3: 2a) of association tracts (left SLF_I, right SLF_II, bilateral ILF, right MLF, left CG, bilateral OR), projection tracts (bilateral CST), and commissural tracts (corpus callosum: anterior midbody, isthmus). In this sub-cluster, significant age-relationships are predominantly observed at high diffusion-weightings where the proportion of variance ranged from 24% to 39%, compared with at low-to-moderate diffusion-weightings (10–28%). The second sub-cluster (Figure 3: 2b) includes cerebellar tracts (MCP, bilateral ICP), rostrum of the corpus callosum, bilateral fornix, right SLF_I and bilateral UF. This represented a sub-cluster of tracts which captured little-to-no variation across development across moderate-low b-values (1–15%).

3.2.3 | Multi-shell multi-tissue FBA

Consistent with the single-shell single-tissue results, sensitivity to age relationships was improved at high diffusion-weightings for multi-shell analyses (Table S1). We observed two main clusters of multi-shell b-value sampling schemes; the first including multiple combinations of low, moderate, and high b-value sampling schemes, and the second including various combinations of high b-value sampling schemes (Figure S5). In addition, we observed two main tract-clusters consistent with the single-tissue results: the first including various left-lateralised association tracts and corpus callosum projections; and the second including predominantly cerebellar tracts, projection tracts (CST) and association tracts (including right SLF_II, SLF_I, ILF, CG, and OR). Overall, we observed a general reduction in the proportion of detectable age-related variance when adding multiple shells for AFD estimation (Figure S5) across various tracts.

### 3.2.4 | Whole brain fixel-based analysis

In order to evaluate the sensitivity of FBA to age-related microstructural development across sampling-schemes, we performed four separate statistical analyses. For each single-shell sampling scheme (b = 1,200; 2,400; 4,000; 6,000 s/mm^2) we tested the relationship between age and AFD using the CFE method (Raffelt et al., 2015).

FBA revealed a significantly positive relationship between AFD and age across all b-values (p_{FWE} < .05). No significant age effects were observed in the opposite direction (p_{FWE} > .05). We observed a general decrease in the number of significant fixels (n_{sig}) when moving from high to low b-values (ss_{6000}: n_{sig} = 13,382; ss_{4000}: n_{sig} = 10,070; ss_{2400}: n_{sig} = 7,283; ss_{1200}: n_{sig} = 5,506). In terms of anatomical overlap between results, 58% of significant fixels overlapped between ss_{6000} and ss_{4000}, 43% of significant fixels overlapped between ss_{6000} and ss_{2400}; and 20% of significant fixels overlapped between ss_{6000} and ss_{1200}. Visualisations of significant and overlapping fixels across diffusion-weightings are depicted in Figure 5. The core regions overlapping across all sampling schemes include the body and splenium of the corpus callosum, left IFOF, left ATR, left SLF, and right CST.

4 | DISCUSSION

In this study we demonstrate a b-value dependence on estimates of apparent fibre density. Our results highlight that AFD more prominently reflects age-related white matter development at high b-values.
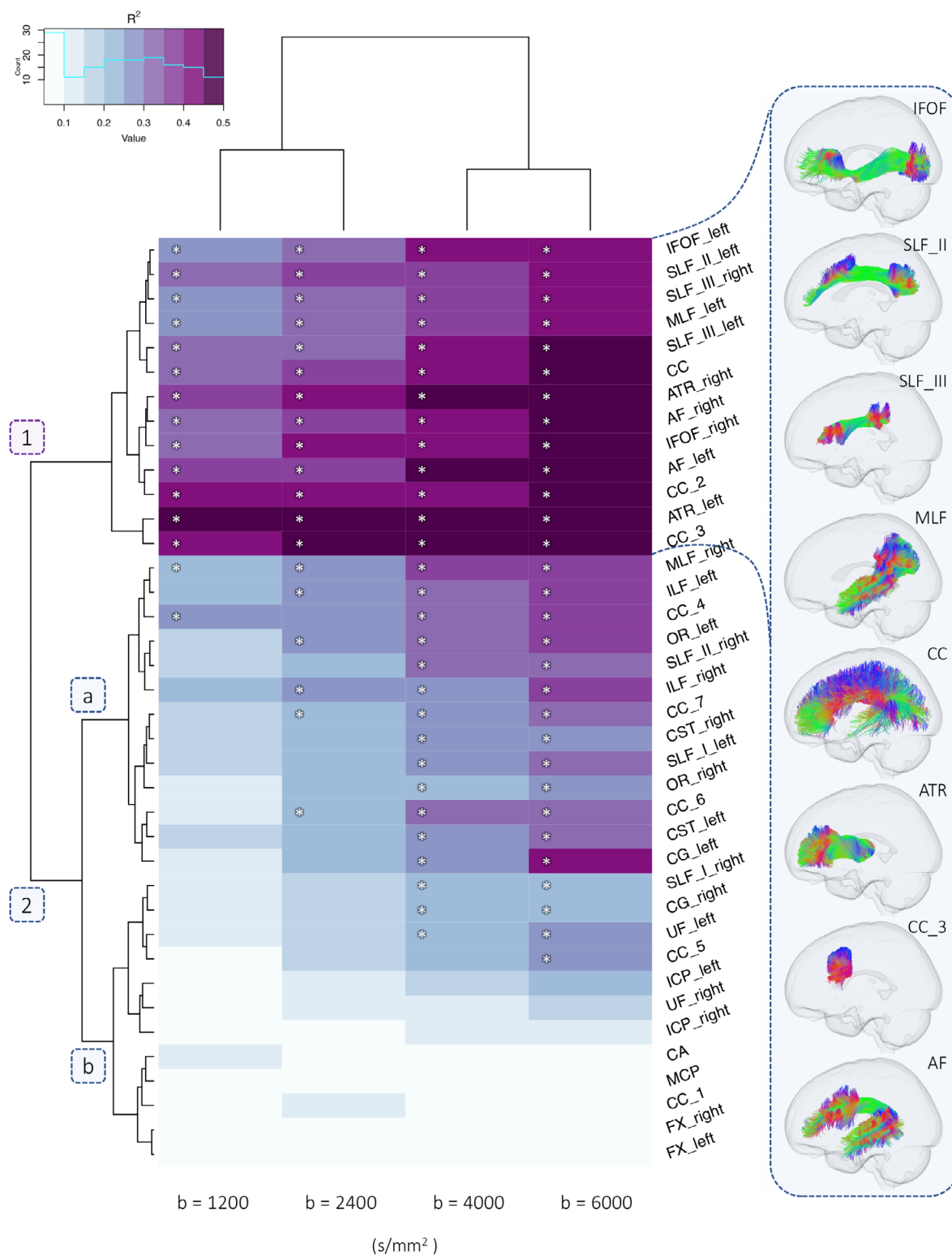
FIGURE 3 Dendrogram heatmap highlighting clusters of tracts which differentially describe age-related differences in apparent fibre density (AFD) across various single-shell b-value sampling schemes. Heatmap colour intensity reflects range of R^2 values derived from a linear model including age, sex, and RMS displacement. Significant age-effects ($p < 3.3e\text{-}4$) are annotated with an asterisk (*). A depiction of several fibre pathways in one cluster is presented on the right

TABLE 1 Variance in AFD explained by age for each single-shell sampling scheme across tracts

| Tracts		R^2				R^2 difference [95% CI]					
		ss_{6000}	ss_{4000}	ss_{2400}	ss_{1200}	$ss_{6000} > ss_{4000}$		$ss_{6000} > ss_{2400}$		$ss_{6000} > ss_{1200}$	
AF	L	.50	.49	.39	.35	.01	[−.11, .06]	.12	[−.01, .18]	**.15**	[.07, .23]
	R	.46	.43	.37	.33	.02	[−.08, .09]	.08	[−.03, .13]	**.13**	[.03, .21]
ATR	L	.53	.50	.43	.42	.03	[−.15, .11]	.11	[−.05, .20]	**.11**	[.02, .27]
	R	.48	.42	.38	.36	.06	[−.01, .13]	**.10**	[.01, .21]	.12	[−.05, .21]
CA		.06	.03	.03	.11	.04	[−.01, .12]	.03	[−.06, .12]	−.05	[−.17, .13]
CC	Full	.44	.39	.32	.31	.04	[−.07, .10]	**.12**	[.03, .20]	.13	[−.04, .21]
	1	.05	.02	.02	.05	.03	[−.04, .13]	.03	[−.04, .17]	.01	[−.12, .14]
	2	.45	.43	.38	.38	.03	[−.13, .10]	.07	[−.07, .17]	.07	[−.04, .19]
	3	.48	.46	.43	.42	.02	[−.03, .07]	**.05**	[.01, .14]	.06	[−.03, .14]
	4	.35	.31	.24	.25	.04	[−.02, .08]	**.11**	[.05, .21]	.10	[−.03, .17]
	5	.22	.16	.11	.06	**.06**	[.02, .10]	**.12**	[.06, .19]	**.16**	[.07, .23]
	6	.34	.29	.21	.14	.04	[−.02, .08]	**.13**	[.07, .20]	**.19**	[.10, .31]
	7	.31	.29	.22	.18	.02	[−.04, .08]	**.09**	[.04, .15]	**.13**	[.05, .20]
CG	L	.38	.27	.18	.10	.11	[−.03, .23]	**.20**	[.06, .34]	**.28**	[.11, .41]
	R	.21	.20	.11	.06	.01	[−.14, .10]	.10	[−.02, .20]	**.16**	[.05, .29]
CST	L	.34	.27	.19	.16	.07	[−.01, .15]	**.15**	[.06, .21]	**.18**	[.05, .27]
	R	.29	.28	.20	.15	.01	[−.08, .09]	.09	[−.01, .17]	**.14**	[.05, .26]
FX	L	.06	.03	.01	.01	.02	[−.04, .10]	.04	[−.02, .12]	.05	[−.01, .16]
	R	.05	.02	.01	.01	.03	[−.04, .10]	.05	[−.04, .16]	.03	[−.12, .18]
ICP	L	.21	.18	.11	.04	.03	[−.01, .14]	**.11**	[.02, .23]	**.17**	[.02, .31]
	R	.11	.11	.07	.08	−.01	[−.07, .07]	.03	[−.07, .14]	.03	[−.10, .16]
IFOF	L	.44	.40	.34	.29	.03	[−.02, .13]	**.10**	[.01, .18]	**.15**	[.09, .26]
	R	.46	.42	.40	.33	.04	[−.02, .12]	.06	[−.01, .14]	**.12**	[.02, .22]
ILF	L	.39	.34	.27	.22	.05	[−.02, .16]	**.13**	[.05, .22]	**.18**	[.10, .27]
	R	.35	.26	.24	.21	**.09**	[.01, .19]	**.10**	[.04, .24]	**.14**	[.05, .25]
MCP		.07	.06	.05	.08	.01	[−.03, .05]	.02	[−.07, .10]	−.02	[−.13, .15]
MLF	L	.43	.39	.30	.26	**.04**	[.01, .09]	**.13**	[.06, .17]	**.17**	[.10, .24]
	R	.39	.34	.28	.20	.05	[−.04, .09]	**.11**	[.02, .18]	**.19**	[.07, .25]
OR	L	.36	.30	.25	.18	**.05**	[.01, .13]	**.11**	[.05, .21]	**.17**	[.10, .28]
	R	.28	.25	.19	.13	.03	[−.04, .10]	**.09**	[.02, .17]	**.15**	[.05, .30]
SLF_III	L	.47	.44	.33	.30	**.04**	[.01, .08]	**.14**	[.08, .19]	**.18**	[.11, .26]
	R	.41	.38	.31	.28	.04	[−.09, .10]	**.10**	[.01, .18]	**.13**	[.01, .24]
SLF_II	L	.41	.40	.32	.29	.01	[−.04, .06]	**.09**	[.02, .14]	**.12**	[.06, .20]
	R	.31	.29	.21	.17	.02	[−.05, .05]	**.10**	[.04, .15]	**.13**	[.07, .22]
SLF_I	L	.29	.24	.19	.15	**.05**	[.01, .11]	**.10**	[.05, .15]	**.14**	[.05, .22]
	R	.22	.20	.15	.08	.02	[−.03, .06]	**.07**	[.02, .13]	**.14**	[.06, .24]
UF	L	.27	.23	.11	.10	.04	[−.05, .16]	**.16**	[.07, .27]	**.16**	[.03, .28]
	R	.17	.09	.04	.04	.08	[−.01, .21]	**.13**	[.03, .26]	**.13**	[.02, .32]

Note: R^2 represents the multiple coefficient of determination computed using a linear model for each tract, with age, sex and motion as predictors. Difference indicates difference between R^2 coefficients. Square brackets show 95% bias corrected accelerated (BCa) confidence intervals computed with 10,000 bootstrapped samples. Bold = differences in R^2 where 0 was not captured by the confidence intervals. Abbreviations: AF, arcuate fasciculus; ATR, anterior thalamic radiation; CA, anterior commissure; CC, corpus callosum [1 = rostrum, 2 = genu, 3 = rostral body, 4 = anterior midbody, 5 = posterior midbody; 6 = isthmus, 7 = splenium]; CG = cingulum; CST, corticospinal tract; FX, fornix; ICP, inferior cerebellar peduncle; IFOF, inferior fronto-occipital fasciculus; ILF, inferior longitudinal fasciculus; MCP, middle cerebellar peduncle; MLF, middle longitudinal fasciculus; OR, optic radiation; superior longitudinal fasciculus: SLF [I, II, III]; UF, uncinate fasciculus.
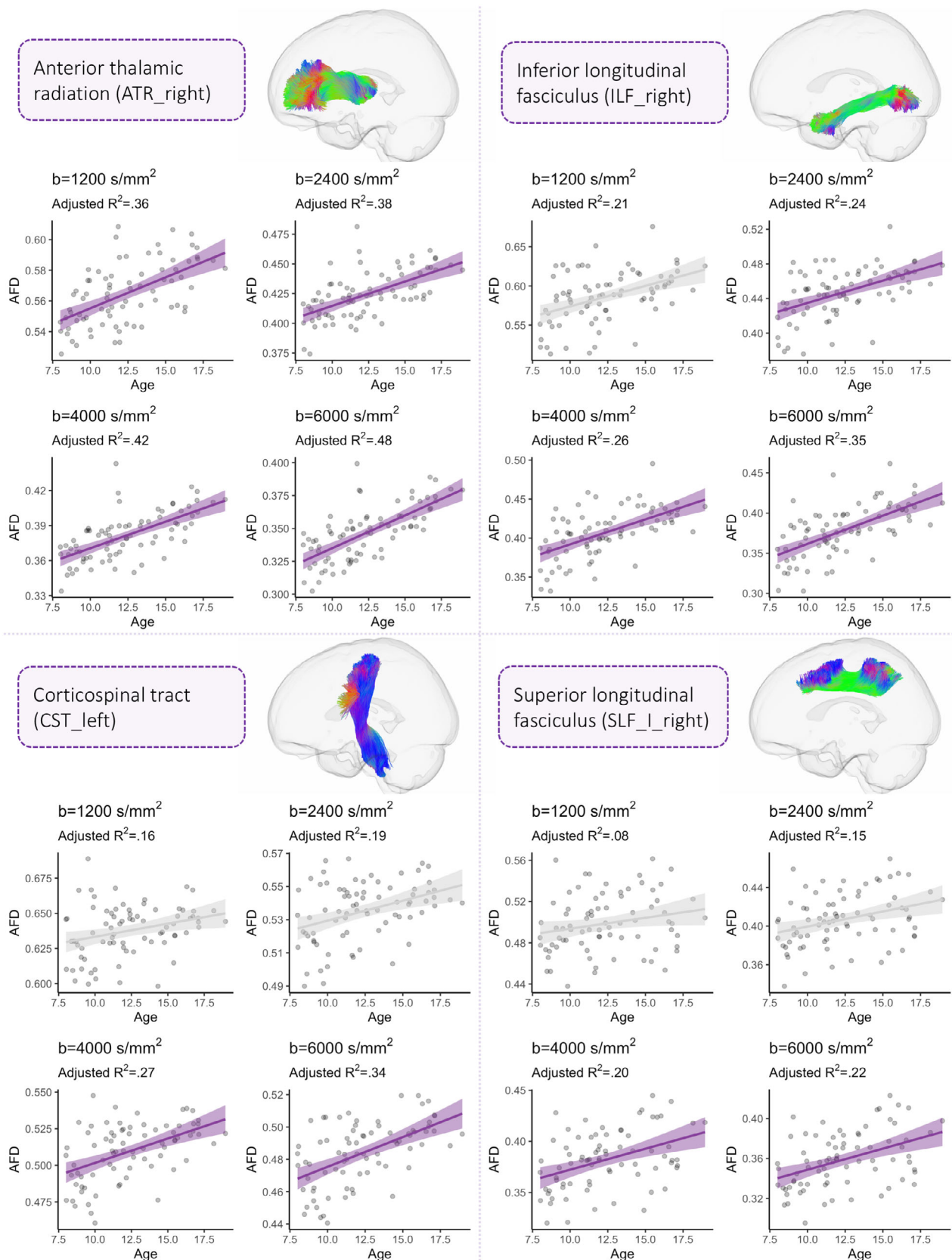
FIGURE 4 The relationship between AFD and age across four regions including: the right anterior thalamic radiation (ATR_right), inferior longitudinal fasciculus (ILF_right), corticospinal tract (CST_left), and superior longitudinal fasciculus I (SLF_I_right). Each region is representative of individual tract clusters where a progressive increase in the coefficient of determination (R^2) is observed when moving from low to high diffusion-weightings. Sampling schemes whereby AFD was significantly associated with age are coloured in purple
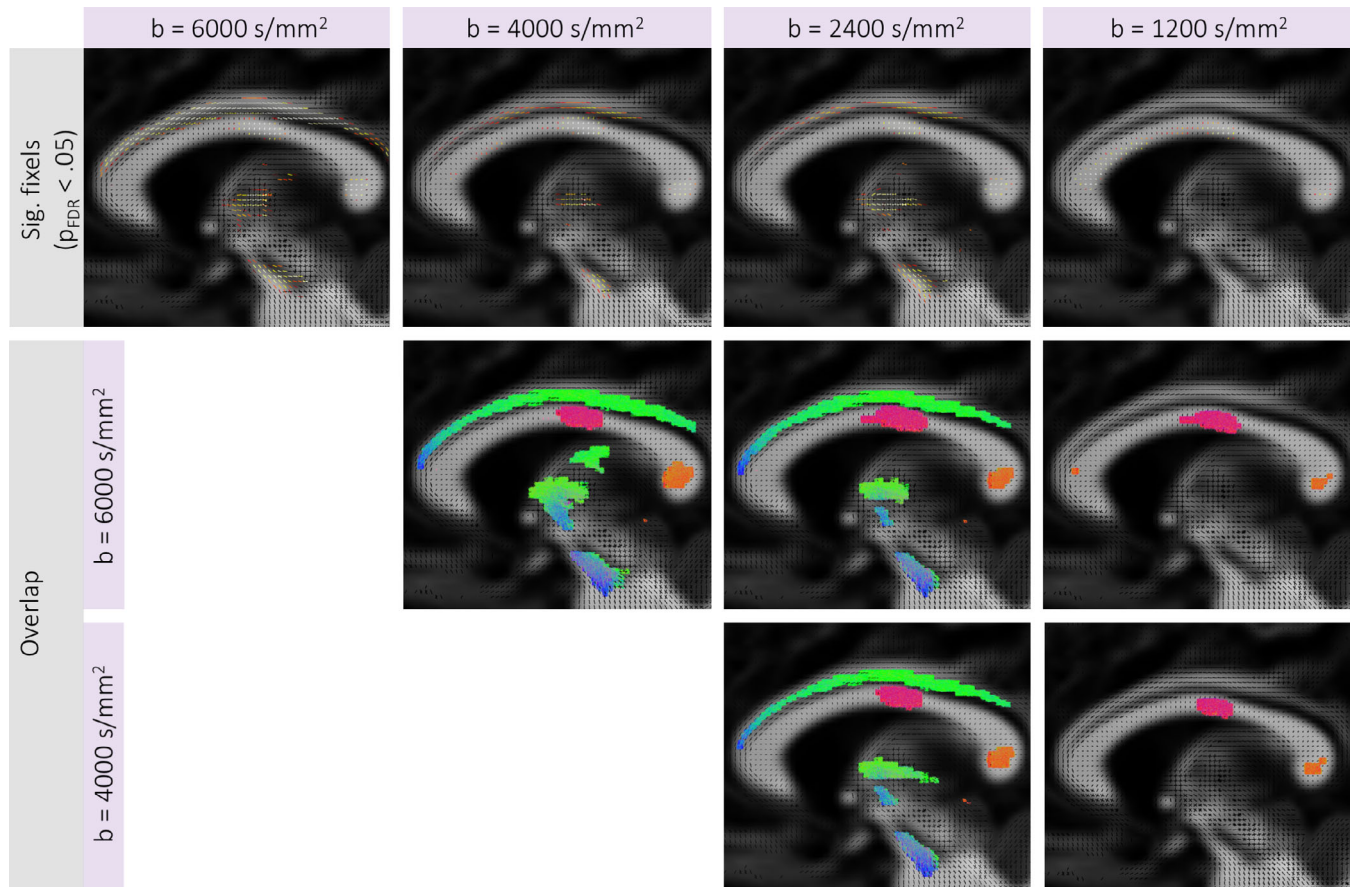
FIGURE 5 Fixel-based analysis results. Top row displays fixels exhibiting a significantly positive relationship between age and AFD for each b-value sampling scheme ($p_{FWE} < .05$). The second (ss_{6000} vs. ss_{4000}; ss_{6000} vs. ss_{2400}; ss_{6000} vs. ss_{1200}) (ss_{4000} vs. ss_{2400}; ss_{4000} vs. ss_{1200}) and third (ss vs. ss; ss vs. ss)(ss_{4000} vs. ss_{2400}) rows display maps of the tracts traversing overlapping fixels between separate FBA results. Results are shown on a representative sagittal slice

4.1 | Simulations

The simulations for multiple sampling schemes revealed an improved correspondence between estimated AFD and the underlying intra-axonal fibre properties when using high b-value shells ($b = 4,000$ or $b = 6,000$ s/mm^2). When moving to lower b-values, or including the complete set of multi-shell data, we observed a larger dependency of AFD on extra-axonal perpendicular diffusivity. This could suggest that any changes in the true underlying fibre density could be camouflaged by concomitant changes in perpendicular diffusivity, whereby a simultaneous reduction of the intra-axonal volume fraction and $D_{e,\perp}$ could result in the AFD remaining the same.

AFD is hypothesised to be proportional to the intra-axonal signal fraction of a fibre population (Raffelt et al., 2012). With increasing b-value, the intra- and extra-axonal signal is differentially attenuated, leading to greater signal contribution from the intra-axonal space (Tournier et al., 2013). Therefore, an increase in AFD can suggest alterations to axonal properties, such as axon count, packing density, and diameter (Raffelt et al., 2017). However, our results suggest that AFD is dependent on the extra-axonal signal when including lower b-values, as the mismatch between estimated

AFD and simulated intra-axonal signal fraction across varying $D_{e,\perp}$ is exaggerated.

As such, a change in AFD estimated at high diffusion-weightings (in this case $b = 4,000$ or $6,000$ s/mm^2) could more directly reflect a change in the underlying axon density compared with lower b-value shells or multi-shell acquisitions, reducing the potential confounding effect of discrepancies with the response function.

4.2 | In vivo developmental data

When considering in vivo developmental data, the dependence of b-value on estimates of AFD was reflected by improved sensitivity to age relationships. Several association tracts consistently described age-related differences in AFD across moderate to high diffusion-weightings, including the left MLF, bilateral IFOF, left SLF II, bilateral SLF III, bilateral ATR, bilateral AF, and anterior segments of the corpus callosum. These regions, particularly the corpus callosum, arcuate and superior longitudinal fasciculus, appear to be sensitive to age-related differences in microstructure regardless of dMRI acquisition scheme or analysis technique (Genc, Smith, et al., 2018;

Ladouceur, Peper, Crone, & Dahl, 2012; Lebel & Beaulieu, 2011; Sawiak et al., 2018).

A group of left-lateralised association tracts (e.g., left CG, MLF, OR, SLF_III, SLF_I, IFOF) better described age-related variance in AFD when comparing the highest b-value (b = 6,000 s/mm^2) with high to moderate b-values (b = 4,000 or 2,400 s/mm^2). Left-lateralisation of language has been well documented (Catani, Jones, & ffytche, 2005) and related to microstructure (Lebel & Beaulieu, 2009). The microstructure of lateralised association tracts is likely linked with the ongoing development of complex cognitive processes throughout childhood and adolescence (Blakemore & Choudhury, 2006; Jung & Haier, 2007). Our results suggest that lateralised association tracts linked with language and cognitive development are better characterised at high b-values. This is likely due to improved sensitivity and specificity to axonal microstructure in the branching endpoints of these tracts integrating such higher order functions across fronto-parietal, fronto-occipital, and occipito-temporal pathways. Future work should focus on investigating subject-specific branching endpoints of these tracts, to assess individual variation in microstructure.

One key observation was that a higher proportion of age-related variance was observed in the single-tissue analyses compared with the multi-tissue analyses. A decrease in discriminative power of age-related development was observed across a number of multi-shell configurations, more heavily weighted towards those which included low-to-moderate b-values. It is possible that single-shell analyses at higher b-values may better isolate the true effect of changing intra-axonal properties, and not clutter it with mismatches of the response function and/or other effects in the extra-axonal space. Future work comparing the current approach with emerging methods such as single-shell three-tissue CSD (Aerts, Dhollander, & Marinazzo, 2019; Dhollander, Mito, Raffelt, & Connelly, 2019) and simultaneous voxel-wise estimation of the response function and FOD (Jespersen et al., 2007) are warranted to explore this further.

The results of the whole-brain FBA revealed a b-value dependence on age-related differences in AFD. Notably, more widespread associations with age were observed at high diffusion-weightings, implicating a number of regions which were not found using other sampling-schemes. This b-value dependence suggests that whilst some core regions such as the body and splenium of the corpus callosum are clearly exhibiting strong age-related development across all sampling schemes, a degree of anatomical sensitivity and specificity is lost at lower diffusion-weightings. This is not to say that studies performing FBA with low-to-moderate b-values will completely lose sensitivity to age-related effects or clinical group differences. However, in conditions with subtle differences in underlying neurobiology or microstructure, going to higher b-values may improve the characterisation of AFD and thus improve the detectability of clinically significant group differences.

Overall, AFD derived from high b-values (b = 4,000 or 6,000 s/mm^2) best modelled age-relationships for the majority of white matter tracts tested. These results, combined with the simulations, suggest that axonal properties (such as axon density) dominate age-related variance in AFD

at high b-values, whereas extra-axonal signal contamination at decreasing diffusion-weightings incrementally suppress this effect.

4.3 | Implications

Our results bear implications for fixel-based analysis applications using retrospectively collected dMRI data which may not be optimal for the estimation of AFD. The biological interpretation of group differences in AFD should be tailored to the acquisition scheme used. Relative differences in AFD at high b-values could relate to the true underlying axon density; at moderate b-values could relate to overall white matter fibre density; and at low b-values could relate to white matter fibre density including potential extra-axonal signal contamination.

Although we have demonstrated a clear b-value dependence on developmental patterns of AFD, it is important to note that the in vivo results at high diffusion-weightings are specific to the ultra-strong gradient system used here, resulting in a higher SNR compared with what could be a achieved on a standard MR system. Promisingly, our simulation results suggest that the effect of b-value and discrepancy with the response function dominates the effect of noise (Figure S3), even at a lower SNR which closely matched our in vivo data (SNR = 50). Therefore, we expect that our observations at high b-values may be reproducible on a standard 3.0T system. As strong gradient systems become increasingly available, the practicalities of acquiring such high quality dMRI data at higher b-values is becoming less cumbersome (Chamberland, Tax, & Jones, 2018; McKinnon & Jensen, 2019; Moss, McKinnon, Glenn, Helpern, & Jensen, 2019).

Whilst in this study we have used a developmental population of children and adolescents as an exemplar of a b-value dependence on estimates of AFD, these findings can be applied more broadly and bear implications for a range of group studies (e.g., clinical groups or ageing adults).

4.4 | Limitations and future directions

One limitation of the current study is that we have no ground truth on the development of axonal density over childhood and adolescence. Therefore, our interpretations of improved intra-axonal signal sensitivity rests on age-relationships investigated here, which has also been used previously (Maximov, Alnæs, & Westlye, 2019; Pines et al., 2019). Whilst we have attempted to understand how AFD can vary across multiple simulated fibre geometries, we do not know how the underlying fibre properties (such as axon diameter) vary with age. Despite this consideration, a recent study of histological validation suggests that AFD is a reliable marker of axonal density in the presence of axonal degeneration (Rojas-Vitea et al., 2019). This is a promising indicator of the neurobiological properties proportional to AFD. Future work should adopt multi-dimensional approaches to extract meaningful components (Chamberland et al., 2019), enhance data

quality (Alexander et al., 2017) and harmonise existing data (Maximov et al., 2019; Tax et al., 2019).

5 | CONCLUSION

We summarise our findings with three main conclusions: (a) the correspondence between apparent fibre density and simulated intra-axonal signal fraction is improved with high *b*-value shells; and (b) AFD better reflects age-related differences in axonal microstructure with increasing *b*-value (b = 4,000 or 6,000 s/mm^2) over childhood and adolescence; and (c) these relationships differ across the brain, with a greater *b*-value dependence in association tracts and posterior projections of the corpus callosum. Together, our results suggest that axonal properties dominate the variance in AFD at high *b*-values.

CONFLICT OF INTEREST

All authors disclose no real or potential conflicts of interest.

DATA AVAILABILITY STATEMENT

The data that support the findings of this study are available on request from the corresponding author. The data are not publicly available due to privacy or ethical restrictions.

ORCID

Sila Genc https://orcid.org/0000-0002-4624-7071

REFERENCES

Aerts, H., Dhollander, T., & Marinazzo, D. (2019). Evaluating the performance of 3-tissue constrained spherical deconvolution pipelines for within-tumor tractography. *bioRxiv*, 629873. https://doi.org/10.1101/629873

Alexander, D. C., Zikic, D., Ghosh, A., Tanno, R., Wottschel, V., Zhang, J., ... Criminisi, A. (2017). Image quality transfer and applications in diffusion MRI. *NeuroImage*, *152*, 283–298.

Andersson, J. L., Skare, S., & Ashburner, J. (2003). How to correct susceptibility distortions in spin-echo echo-planar images: Application to diffusion tensor imaging. *NeuroImage*, *20*, 870–888.

Andersson, J. L. R., & Sotiropoulos, S. N. (2016). An integrated approach to correction for off-resonance effects and subject movement in diffusion MR imaging. *NeuroImage*, *125*, 1063–1078.

Avants, B. B., Tustison, N. J., Song, G., Cook, P. A., Klein, A., & Gee, J. C. (2011). A reproducible evaluation of ANTs similarity metric performance in brain image registration. *NeuroImage*, *54*, 2033–2044.

Barth, M., Breuer, F., Koopmans, P. J., Norris, D. G., & Poser, B. A. (2016). Simultaneous multislice (SMS) imaging techniques. *Magnetic Resonance in Medicine*, *75*, 63–81.

Blakemore, S. J., & Choudhury, S. (2006). Development of the adolescent brain: Implications for executive function and social cognition. *Journal of Child Psychology and Psychiatry, and Allied Disciplines*, *47*, 296–312.

Caruyer, E., Lenglet, C., Sapiro, G., & Deriche, R. (2013). Design of multi-shell sampling schemes with uniform coverage in diffusion MRI. *Magnetic Resonance in Medicine*, *69*, 1534–1540.

Catani, M., Jones, D. K., & ffytche, D. H. (2005). Perisylvian language networks of the human brain. *Annals of Neurology*, *57*, 8–16.

Chamberland, M., Raven, E. P., Genc, S., Duffy, K., Descoteaux, M., Parker, G. D., ... Jones, D. K. (2019). Dimensionality reduction of diffusion MRI measures for improved tractometry of the human brain. *NeuroImage*, *200*, 89–100.

Chamberland, M., Tax, C. M. W., & Jones, D. K. (2018). Meyer's loop tractography for image-guided surgery depends on imaging protocol and hardware. *Neuroimage: Clinical*, *20*, 458–465.

Dell'Acqua, F., Simmons, A., Williams, S. C., & Catani, M. (2013). Can spherical deconvolution provide more information than fiber orientations? Hindrance modulated orientational anisotropy, a true-tract specific index to characterize white matter diffusion. *Human Brain Mapping*, *34*, 2464–2483.

Dell'Acqua, F., & Tournier, J. D. (2019). Modelling white matter with spherical deconvolution: How and why? *NMR in Biomedicine*, *32*, e3945.

Dhollander, T., Mito, R., Raffelt, D., & Connelly, A. Improved white matter response function estimation for 3-tissue constrained spherical deconvolution. 0555. In 2019; Montreal, Canada.

Dhollander, T., Raffelt, D., & Connelly, A. Unsupervised 3-tissue response function estimation from single-shell or multi-shell diffusion MR data without a co-registered T1 image. 2016.

Dimond, D., Schuetze, M., Smith, R. E., Dhollander, T., Cho, I., Vinette, S., ... Bray, S. (2019). Reduced white matter fiber density in autism spectrum disorder. *Cerebral Cortex*, *29*, 1778–1788.

Dyrby, T. B., Lundell, H., Burke, M. W., Reislev, N. L., Paulson, O. B., Ptito, M., & Siebner, H. R. (2014). Interpolation of diffusion weighted imaging datasets. *NeuroImage*, *103*, 202–213.

Fieremans, E., Jensen, J. H., & Helpern, J. A. (2011). White matter characterization with diffusional kurtosis imaging. *NeuroImage*, *58*, 177–188.

Gajamange, S., Raffelt, D., Dhollander, T., Lui, E., van der Walt, A., Kilpatrick, T., ... Kolbe, S. (2018). Fibre-specific white matter changes in multiple sclerosis patients with optic neuritis. *Neuroimage Clinical*, *17*, 60–68.

Genc, S., Malpas, C. B., Ball, G., Silk, T. J., & Seal, M. L. (2018). Age, sex, and puberty related development of the corpus callosum: A multi-technique diffusion MRI study. *Brain Structure & Function*, *223*, 2753–2765.

Genc, S., Smith, R. E., Malpas, C. B., Anderson, V., Nicholson, J. M., Efron, D., ... Silk, T. J. (2018). Development of white matter fibre density and morphology over childhood: A longitudinal fixel-based analysis. *NeuroImage*, *183*, 666–676.

Genc, S., Tax, C. M., Raven, E. P., Chamberland, M., Parker, G. D., & Jones, D.K. New insights into the development of white matter microstructure across childhood and adolescence from ultra-strong gradients. 0381. In 2019; Montreal, Canada. p 0381.

Glasser, M. F., Sotiropoulos, S. N., Wilson, J. A., Coalson, T. S., Fischl, B., Andersson, J. L., ... Jenkinson, M. (2013). The minimal preprocessing pipelines for the human connectome project. *NeuroImage*, *80*, 105–124.

Jespersen, S. N., Kroenke, C. D., Ostergaard, L., Ackerman, J. J., & Yablonskiy, D. A. (2007). Modeling dendrite density from magnetic resonance diffusion measurements. *NeuroImage*, *34*, 1473–1486.

Jeurissen, B., Tournier, J. D., Dhollander, T., Connelly, A., & Sijbers, J. (2014). Multi-tissue constrained spherical deconvolution for improved analysis of multi-shell diffusion MRI data. *NeuroImage*, *103*, 411–426.

Jones, D. K., Alexander, D. C., Bowtell, R., Cercignani, M., Dell'Acqua, F., McHugh, D. J., ... Tax, C. M. W. (2018). Microstructural imaging of the human brain with a 'super-scanner': 10 key advantages of ultra-strong gradients for diffusion MRI. *NeuroImage*, *182*, 8–38.

Jones, D. K., Horsfield, M. A., & Simmons, A. (1999). Optimal strategies for measuring diffusion in anisotropic systems by magnetic resonance imaging. *Magnetic Resonance in Medicine*, *42*, 515–525.

Jung, R. E., & Haier, R. J. (2007). The Parieto-frontal integration theory (P-FIT) of intelligence: Converging neuroimaging evidence. *The Behavioral and Brain Sciences*, *30*, 135–154 discussion 154-87.

Kellner, E., Dhital, B., Kiselev, V. G., & Reisert, M. (2016). Gibbs-ringing artifact removal based on local subvoxel-shifts. *Magnetic Resonance in Medicine*, *76*, 1574–1581.

Kroenke, C. D., Ackerman, J. J. H., & Yablonskiy, D. A. (2004). On the nature of the NAA diffusion attenuated MR signal in the central nervous system. *Magnetic Resonance in Medicine*, *52*, 1052–1059.

Kunz, N., Zhang, H., Vasung, L., O'Brien, K. R., Assaf, Y., Lazeyras, F., ... Hüppi, P. S. (2014). Assessing white matter microstructure of the newborn with multi-shell diffusion MRI and biophysical compartment models. *NeuroImage*, *96*, 288–299.

Ladouceur, C. D., Peper, J. S., Crone, E. A., & Dahl, R. E. (2012). White matter development in adolescence: The influence of puberty and implications for affective disorders. *Developmental Cognitive Neuroscience*, *2*, 36–54.

Landman, B. A., Farrell, J. A. D., Jones, C. K., Smith, S. A., Prince, J. L., & Mori, S. (2007). Effects of diffusion weighting schemes on the reproducibility of DTI-derived fractional anisotropy, mean diffusivity, and principal eigenvector measurements at 1.5T. *NeuroImage*, *36*, 1123–1138.

Le Bihan, D., & Breton, E. (1985). In vivo magnetic resonance imaging of diffusion. *Comptes Rendus Des Seances de l'Academie Des Sciences Serie*, *2*(301), 1109–1112.

Lebel, C., & Beaulieu, C. (2009). Lateralization of the arcuate fasciculus from childhood to adulthood and its relation to cognitive abilities in children. *Human Brain Mapping*, *30*, 3563–3573.

Lebel, C., & Beaulieu, C. (2011). Longitudinal development of human brain wiring continues from childhood into adulthood. *The Journal of Neuroscience: The Official Journal of the Society for Neuroscience*, *31*, 10937–10947.

Lebel, C., & Deoni, S. (2018). The development of brain white matter microstructure. *NeuroImage*, *182*, 207–218.

Maximov, I. I., Alnæs, D., & Westlye, L. T. (2019). Towards an optimised processing pipeline for diffusion magnetic resonance imaging data: Effects of artefact corrections on diffusion metrics and their age associations in UKbiobank. *Human Brain Mapping*, *40*(14), 4146–4162.

McKinnon, E. T., & Jensen, J. H. (2019). Measuring intra-axonal T2 in white matter with direction-averaged diffusion MRI. *Magnetic Resonance in Medicine*, *81*, 2985–2994.

Mito, R., Raffelt, D., Dhollander, T., Vaughan, D. N., Tournier, J. D., Salvado, O., ... Connelly, A. (2018). Fibre-specific white matter reductions in Alzheimer's disease and mild cognitive impairment. *Brain*, *141*, 888–902.

Moss, H., McKinnon, E. T., Glenn, G. R., Helpern, J. A., & Jensen, J. H. (2019). Optimization of data acquisition and analysis for fiber ball imaging. *NeuroImage*, *200*, 690–703.

Novikov, D. S., Veraart, J., Jelescu, I. O., & Fieremans, E. (2018). Rotationally-invariant mapping of scalar and orientational metrics of neuronal microstructure with diffusion MRI. *NeuroImage*, *174*, 518–538.

Pines, A. R., Cieslak, M., Baum, G. L., Cook, P. A., Adebimpe, A., Davila, D. G., ... Satterthwaite, T. D. (2019). Advantages of multi-shell diffusion models for studies of brain development in youth. *bioRxiv*, 611590. https://doi.org/10.1101/611590

Raffelt, D., Tournier, J. D., Rose, S., Ridgway, G. R., Henderson, R., Crozier, S., ... Connelly, A. (2012). Apparent fibre density: A novel measure for the analysis of diffusion-weighted magnetic resonance images. *NeuroImage*, *59*, 3976–3994.

Raffelt, D. A., Smith, R. E., Ridgway, G. R., Tournier, J. D., Vaughan, D. N., Rose, S., ... Connelly, A. (2015). Connectivity-based fixel enhancement: Whole-brain statistical analysis of diffusion MRI measures in the presence of crossing fibres. *NeuroImage*, *117*, 40–55.

Raffelt, D. A., Tournier, J. D., Smith, R. E., Vaughan, D. N., Jackson, G., Ridgway, G. R., & Connelly, A. (2017). Investigating white matter fibre density and morphology using fixel-based analysis. *NeuroImage*, *144*, 58–73.

Raven, E. P., Chamberland, M., Genc, S., Duffy, K., Tax, C. M., Parker, G. D., ..., Jones, D. K. Gradient profiles of myelin and microstructure metrics across the developing brain. 2618. In 2019; Montreal, Canada.

Rojas-Vitea, G., Coronado-Leijaa, R., Narvaez-Delgado, O., Ramírez-Manzanares, A., Marroquín, J. L., Noguez-Imm, R., ... Conchaa, L. (2019). Histological validation of per-bundle water diffusion metrics within a region of fiber crossing following axonal degeneration. *Neuroimage*, *201*, 116013.

Rudrapatna, S., Parker, G., Roberts, J., & Jones, D. Can we correct for interactions between subject motion and gradient-nonlinearity in diffusion MRI. 2018.

Sairanen, V., Leemans, A., & Tax, C. M. W. (2018). Fast and accurate Slicewise OutLIer detection (SOLID) with informed model estimation for diffusion MRI data. *NeuroImage*, *181*, 331–346.

Sawiak, S. J., Shiba, Y., Oikonomidis, L., Windle, C. P., Santangelo, A. M., Grydeland, H., ... Roberts, A. C. (2018). Trajectories and milestones of cortical and subcortical development of the marmoset brain from infancy to adulthood. *Cerebral Cortex*, *28*(12), 4440–4453.

Silk, T. J., Genc, S., Anderson, V., Efron, D., Hazell, P., Nicholson, J. M., ... Sciberras, E. (2016). Developmental brain trajectories in children with ADHD and controls: A longitudinal neuroimaging study. *BMC Psychiatry*, *16*, 59.

Smith, S. M., Jenkinson, M., Woolrich, M. W., Beckmann, C. F., Behrens, T. E., Johansen-Berg, H., ... Matthews, P. M. (2004). Advances in functional and structural MR image analysis and implementation as FSL. *NeuroImage*, *23*(Suppl. 1), S208–S219.

Somerville, L. H., Bookheimer, S. Y., Buckner, R. L., Burgess, G. C., Curtiss, S. W., Dapretto, M., ... Barch, D. M. (2018). The lifespan human connectome project in development: A large-scale study of brain connectivity development in 5-21 year olds. *NeuroImage*, *183*, 456–468.

Tax, C. M. W., Grussu, F., Kaden, E., Ning, L., Rudrapatna, U., John Evans, C., ... Veraart, J. (2019). Cross-scanner and cross-protocol diffusion MRI data harmonisation: A benchmark database and evaluation of algorithms. *NeuroImage*, *195*, 285–299.

Tax, C. M. W., Jeurissen, B., Vos, S. B., Viergever, M. A., & Leemans, A. (2014). Recursive calibration of the fiber response function for spherical deconvolution of diffusion MRI data. *NeuroImage*, *86*, 67–80.

Tournier, J. D., Calamante, F., & Connelly, A. (2007). Robust determination of the fibre orientation distribution in diffusion MRI: Non-negativity constrained super-resolved spherical deconvolution. *NeuroImage*, *35*, 1459–1472.

Tournier, J. D., Calamante, F., & Connelly, A. (2013). Determination of the appropriate b value and number of gradient directions for high-angular-resolution diffusion-weighted imaging. *NMR in Biomedicine, 26,* 1775–1786.

Tournier, J. D., Mori, S., & Leemans, A. (2011). Diffusion tensor imaging and beyond. *Magnetic Resonance in Medicine, 65,* 1532–1556.

Tournier, J. D., Smith, R. E., Raffelt, D. A., Tabbara, R., Dhollander, T., Pietsch, M., … Connelly, A. (2019). MRtrix3: A fast, flexible and open software framework for medical image processing and visualisation. *NeuroImage, 202,* 116137.

Tustison, N. J., Avants, B. B., Cook, P. A., Zheng, Y., Egan, A., Yushkevich, P. A., & Gee, J. C. (2010). N4ITK: Improved N3 bias correction. *IEEE Transactions on Medical Imaging, 29,* 1310–1320.

Veraart, J., Fieremans, E., & Novikov, D. S. (2016). Diffusion MRI noise mapping using random matrix theory. *Magnetic Resonance in Medicine, 76,* 1582–1593.

Vos, S. B., Tax, C. M., Luijten, P. R., Ourselin, S., Leemans, A., & Froeling, M. (2017). The importance of correcting for signal drift in diffusion MRI. *Magnetic Resonance in Medicine, 77,* 285–299.

Warnes, G. R., Bolker, B., Bonebakker, L., Gentleman, R., Liaw, W. H. A., Lumley, T., … Venables, B. 2015. *gplots: Various R Programming Tools for Plotting Data. Version R package version 2.17.0.* https://www.scienceopen.com/document?vid=0e5d8e31-1fe4-492f-a3d8-8cd71b2b8ad9

Wasserthal, J., Neher, P., & Maier-Hein, K. H. (2018). TractSeg – Fast and accurate white matter tract segmentation. *NeuroImage, 183,* 239–253.

Wasserthal, J., Neher, P. F., Hirjak, D., & Maier-Hein, K. H. (2019) Combined tract segmentation and orientation mapping for bundle-specific tractography. *arXiv [cs.CV],* 1901.10271.

Zhang, H., Schneider, T., Wheeler-Kingshott, C. A., & Alexander, D. C. (2012). NODDI: Practical in vivo neurite orientation dispersion and density imaging of the human brain. *NeuroImage, 61,* 1000–1016.

SUPPORTING INFORMATION

Additional supporting information may be found online in the Supporting Information section at the end of this article.